Nanoscale

PAPER

View Article Online
View Journal | View Issue

Cite this: *Nanoscale*, 2025, **17**, 23612

Nanoscale imaging and atomic vibrations of eumelanin superstructures modulated by functionalized micronized graphene oxide

Roberto Matassa, *[a,b] Sara Mattiello, [a] Gustavo Guerreiro Candido Soares,[c] Juan G. Lozano, [d] Ana M. Beltrán, [d] Costantino Zazza, [e] Nico Sanna, [e] Jun Wei Phua, [f] Jose Mauricio Rosolen, [c] Andrea Di Cicco, [a] Javad Rezvani [a] and Roberto Gunnella [a]

Natural organic/inorganic materials with rational cooperative formations have long been of enormous interest owing to their hybrid self-assembling properties. Natural biomolecules are expected to produce attractive superstructures capable of sensing their environment, following their inherent biological functions and high biocompatibility. However, understanding their assembly strategies with inorganic materials is often challenging. Herein, we investigated the bioactive assembly of natural eumelanin superstructures. modulated by chemical functionalization of micronized graphene oxide, to study their strong structural affinity by analysing their vibrational–structural correlations. The application of complementary experiments of high-resolution electron nanoimaging coupled with vibrational Raman spectroscopy revealed intriguing and unique features of this complex hybrid material. In particular, high-resolution nanodiffraction/imaging analysis provided evidence of new nanocrystalline domains of pure natural eumelanin with different and irregular orientations forming irregular nanosheets. Interestingly, a hierarchical reassembly process of eumelanin units are actually evident not only on the oxide graphene surface but also located in high amounts on the edge of vertical graphene oxide, concretely supported by the analytical changes of the predominant resonance bands (D, D**, and G). This confirmed the ability of eumelanin to reassemble in spherical and elongated nanostructures when induced by an external stimuli of graphene oxide in an aqueous solution at room temperature. Thus, this work highlights the assembling mechanisms for designing a strategy to control bioactive molecules through environment modification.

Received 14th June 2025,
Accepted 5th September 2025

DOI: 10.1039/d5nr02546j

rsc.li/nanoscale

1. Introduction

Living systems are abundant in oxygen, carbon and hydrogen, which are organized in highly hierarchical structures. This complexity arises from the versatile chemistry of the carbon element, which enables the formation of superstructures held together by covalent bonds and/or the incorporation of oxygen-containing functionalities. These multidimensional superstructures with complex conformations, particularly the small biomolecular units, are known to be modulated through mutual interactions with their nanoenvironment, which is full of functional, flexible, and complex components.[1] This dynamic self-assembly commonly observed in biological living systems can also appear in inorganic materials. One promising material platform is micronized graphene oxide (GO_m) since it has dimensions and chemical compositions similar to cells, bringing this inanimate material to the boundary between living organic and inorganic systems. The biocompatible graphene oxide surface exhibits high flexibility in forming biological-inorganic superstructures, enabled by localized functionalities at the atomic scale.[2] However, control over the contact interface is achieved using simpler strategies that are evolved in living systems, such as controlled assembly. This implies that an active biosystem capable of reacting to multiple inputs

[a]*Physics Division, School of Science and Technology, University of Camerino, 62032 Camerino, Macerata, Italy. E-mail: roberto.matassa@unicam.it*
[b]*Department of Anatomical, Histological, Forensic and Orthopaedic Sciences, Section of Human Anatomy, Sapienza University of Rome, Via A. Borelli 50, 00161 Rome, Italy. E-mail: roberto.matassa@uniroma1.it*
[c]*Departamento de Química, Faculdade de Filosofia, Ciências e Letras de Ribeirão Preto, Universidade de São Paulo, Av. Bandeirantes 3900, 14040-901 Ribeirão Preto, Brazil*
[d]*Departamento de Ingeniería y Ciencia de los Materiales y del Transporte, Escuela Técnica Superior de Ingeniería y Escuela Politécnica Superior, Universidad de Sevilla, 41092 Seville, Spain*
[e]*Department for Innovation in Biological, Agro-food and Forest systems, Università della Tuscia (DIBAF), L.go dell'Università s.n.c., 01100 Viterbo, Italy*
[f]*Insectta Pte. Ltd, 8 Cleantech Loop, Singapore, 637145, Singapore*

is dependent on both the binding of a small molecule and the engagement of functionalized carbon. One promising candidate is the pigment eumelanin (*e*Mel), which is abundant in nature and among the smallest active biomolecules. This melanin-like material shows broadband optical absorption, a useful property for human photoprotection, with a negligible energy gap and low radiative quantum yield. Eumelanin shows notable excitation energies at specific incoming wavelengths, yet its fluorescence is confined to a relatively fixed energy range.[3] This relatively complex excitation–emission behaviour has been attributed to the poor long-range crystalline order of the *e*Mel molecules, as evidenced by wide- and small-angle X-ray diffraction studies, which yield diverse morpho-structural interpretations.[4,5] The possible existence of short-range crystalline order, which is not yet experimentally observed in *e*Mel, may be associated with bifurcated hydrogen bondings, which are theoretically presumed to strongly interact with other hydroxyl systems (O–H···O).[6]

The control over the chemical functionalization of eumelanin with the strong absorptive properties of GO_m substrates could result in the development of a hybrid nanoscale device. Indeed, the assembly of possible sp^n hybridizations of this inorganic-biological system offers the opportunity to tailor the electronic and structural properties, enabling enhanced or combined mechanical strength, conductivity, and photon absorption over a wide range of wavelengths.[7,8] To make an impact on research and real technological applications, a key issue is the identification of highly sustainable, low-cost, and scalable production of the hybrid assembly processes, such as eumelanin extracted from the black soldier fly,[6,9] and the low-cost GO_m.[7] However, the removal of p_z orbitals from the π-system in graphene oxide, which is manufactured by creating atomic vacancies or adsorbing functional groups in a controlled manner, remains a challenge. Changing the initial sp^2 hybridization to essentially sp^3 involves zig-zag edges, grain boundaries, and atomic defects, which experimentally appear to be randomly distributed on the GO_m sheets.[10,11] For these reasons, the morpho-structural arrangements of the modified graphene sheets, affected by bending, curving, and wrinkling formations, have been characterized at the nanometric scale by direct microscopy imaging techniques.[12,13] Other indirect structural investigations, based on experimental and theoretical spectroscopies, revealed atomic defect sites on both surface and expanded edges that modulated the order/disorder of the sheet arrangements.[14,15] The interesting advantage of this layered material is the preserved threefold symmetry of the graphene atomic lattice, which favours the physi-chemisorption of different active small species, in order to tune their hybrid physicochemical properties. A key issue for such applications is the determination of the possible hybrid interactions in order to reveal the open opportunities and the limitations posed, which are directly dependent on the size-spatial distribution of *e*Mel on the two-dimensional structure of GO_m. Thus, expanding the study of micronized graphene oxide with the design flexibility of the organic eumelanin at both the molecular and atomic levels remains a considerable challenge, broadening the scope of scientific research beyond traditional methodological investigations.[16] In particular, it remains unclear why the smallest structural units of eumelanin, such as those with possible long-range and/or short-range ordered crystal lattices, often exhibit different nanometric morphologies, dependent on the extraction methods from different natural products.[17] Furthermore, a precise understanding of the short-range morpho-structural changes of eumelanin, which rearrange dynamically in response to the inputs, remains elusive.

For these reasons, the advancement of inorganic–biological synthesis approaches requires precise characterization techniques capable of revealing nanoscale details, in order to better understand the fundamental self-assembly mechanisms in inorganic–biological materials. Since the structural properties of hybrid materials are strongly dependent on the size, shape, crystalline structure, and composition of the materials involved, an ensemble of electron microscopy techniques is necessary to fully characterize the morpho-structural properties of this inorganic–organic assembly. Despite being a powerful tool for structural characterization, the application of high-resolution TEM (HR-TEM) can induce radiation damage in a wide range of materials due to exposure to the electron beam. Therefore, Raman spectroscopy may provide new insights into the atomic-scale behaviour of the materials, overcoming the limitations of HR-TEM, and revealing the organic molecular structures and their interactions. Resonance micro-Raman scattering with high spatial resolution provides information about atomic defects, as well as the order/disorder molecular stacking, which depends on the mutual orientation between crystal size and polarization directions of the excitation wavelength.[18] However, the conventional vibrational Raman spectroscopy typically averages information over much larger length scales, while the energy resolution remains unmatched compared to that of high-resolution electron imaging/spectroscopy. Therefore, the combination of localized atomic vibrational data with the morpho-structural data obtained by high-resolution electron microscopy might provide a fingerprint for studying organic–inorganic interactions.[19,20]

Herein, we report vibrational–structural analyses of the effects of changes in the eumelanin molecular organization on the surface/bulk structural properties, influenced by the structural environment of defect micronized graphene oxide. This work aims at integrating morpho-structural-vibrational information through a methodology designed to assemble small eumelanin units into superaggregates, an effect driven by the defects present in the graphene oxide layers, which can be used to tailor the optoelectronic properties of complex hybrid materials.[21] To obtain insights into these intriguing and complex hybrid biomaterials, a combination of Raman spectroscopy and electron microscopy imaging, supported by quantitative data/imaging analyses, has been used with the following objectives: (i) to investigate morpho-vibrational relationships in GO_m, *e*Mel, and GO_m–*e*Mel by coupling TEM-Raman microscopy techniques (Fig. 1); (ii) to analyse the full morpho-

structural properties of micronized graphene oxide, showing twisting, wrinkling, folding, and atomic defect formations (Fig. 2); (iii) to image direct evidence of the short-range crystalline order in *e*Mel (Fig. 3); (iv) and to monitor the changes in the short-range order of the eumelanin molecular units modulated by oxygen-containing functional groups of defect micronized graphene oxide (Fig. 4). Synergistically integrating the outcomes of the above scientific objectives is crucial for understanding the directed assembly of novel nanoarchitectures through chemical functionalization and the hierarchical organization of biological materials with inanimate carbon structures.[22]

2. Results and discussion

2.1. Morpho-vibrational behaviour from micron to atomic-length scale

Direct imaging of graphene oxide in micronized dimensions (GO_m) revealed distinct interactions with eumelanin molecules, where structural reorganizations depend on surface and edge defects in GO_m. To gain insight into the self-assembly behaviour of the proposed inorganic–organic system at the nanoscale, high-resolution electron microscopy techniques (HRTEM, SAED, and EDX spectroscopy) were employed to obtain all comprehensive experimental findings (Fig. 1–4). Further information on the presence of different oxidation interactions, structural defects, and crystalline domains of such a hybrid system has been gathered using image analysis of nano-areas through sequences of Fast Fourier Transforms (FFTs) and Inverse Fast Fourier Transforms (IFFTs).[20,23]

However, due to the well-known limitations of high-resolution TEM to image the crystalline lattice of soft biomaterials, this technique needs to be combined with Raman spectroscopy at the atomic-length scale. These complementary experiments of conventional microscopies require an approach to integrate and analyze imaging data to define the fine relationships between the structure and the essential interactions of these complex hybrid nanostructures. A first combination of these techniques with complementary spatial resolutions to understand the morpho-vibrational behaviors of micronized graphene oxide, eumelanin, and their hybrid interactions is summarized in Fig. 1.

2.2. Direct vibrational–structural relationships in micronized graphene oxide

The bright-field TEM image of a GO_m sheet affected by bending, curving, and wrinkling formations with the highest electron transparency, even in comparison to the thin-film carbon support, is shown in Fig. 1a. Morphometric characterization shows the micronized nature of the GO_m with an area of 8.38 μm^2 and a planar dimension of about 3.79 μm. The O peak in the corresponding EDX spectrum (inset) confirms the presence of robust oxidation. The probed micro-Raman first-order spectral region, ranging from 500 to 1900 cm^{-1}, exhibits the typical D, G, and the hidden deconvoluted D* and D′ bands (see Fig. 1a-R_I, Table S1). To study the chemical bond behaviours at the surface and edge, the D and G bands centered at 1.352 and 1.589 cm^{-1}, typical of carbon derivatives, arise from disordered graphitic materials and sp^2-hybridized carbon systems, respectively.[24] The D broad band, which is relatively intense compared to the G band, exhibits an estimated relative D-to-G intensity ratio of 1.09, implying the presence of short-range crystallinity order (Fig. 1a) surrounded by atomic defects, especially near the surface.[25] Indeed, the small crystalline planar size *La* of about 17.80 nm, inversely proportional to the intensity ratio, was estimated by including the experimental laser excitation energy.[15] The disorder-induced structure generated by irregular self-aggregation due to the hydrogenated and oxide carbon defects can be observed directly in the inset of Fig. 1a (see the SI). Chemical–structural disorder coming from planar structural defects has been well-recognized in their different chemical vibration bonds by analysing the deconvoluted hidden peaks of the Raman spectra.[26] The middle band (D**) of a deconvolved peak at about 1491 cm^{-1} was estimated; in this context, such a band is related to the edge plane of disordered pyrolytic graphite due to the (C═C) stretching of sp^2 hybridization and δ(C–H) bending modes of hydrogenated carbons.[27,28] The further D′ band found at about 1608 cm^{-1}, partially merged with the G band, arises from the C–O stretching modes at the edge, and from the surface hexagonal carbon rings generating short-range crystallinity order.[8,11] Further bond vibrations of visible excitations obtained from the deconvoluted peaks at about 1129 and 1255 cm^{-1}, not measured in pristine crystal graphite, were observed in defect graphite and graphene oxide structures.[15] Both modes assigned to the D* broad band have been assigned to the C–OH and C–C stretching vibrations of hydrogenated and not hydrogenated sp^3 sites.[29]

Due to the broadening of first-order Raman peaks caused by atomic disorder—such as variations in bond lengths, bond angles, and functionalization—the Raman spectral range of the inorganic and/or organic species was extended to 2000–3500 cm^{-1} frequencies.[30] The identified combinations between the fundamental modes are active in D + D″, 2D, D + D′, 2G, and 2D′ bands, providing information on the lattice dynamics of graphitized materials (Fig. 1a-R_{II}, Table S1). The sum of the D″ and D modes, not detected in GO_m, can be associated with the D + D″ graphite band near 2462 cm^{-1}, as an identification of finite-size crystals (nano-islands).[27,30] Among the measured overtone peaks of the GO_m, the most intense broad band exhibited a 2D band (2680 cm^{-1}), which confirmed the presence of turbostratic or twisted sheets, and therefore a low crystallinity order (Fig. 2). This band represents an advantage to determine nanocrystal arrangements that may have a non-defect twisted assembly since the resonance of the 2D and 2D′ (~3393 cm^{-1}) peaks is independent of the D peak. This is because the activation of two phonons with the same momentum is not required.[31] Instead, the combination of phonons with different momenta of the D + D′ band (~2944 cm^{-1}), observed previously in graphene whiskers,[18] requires atomic defects for its activation.[14] Lastly, the overtone

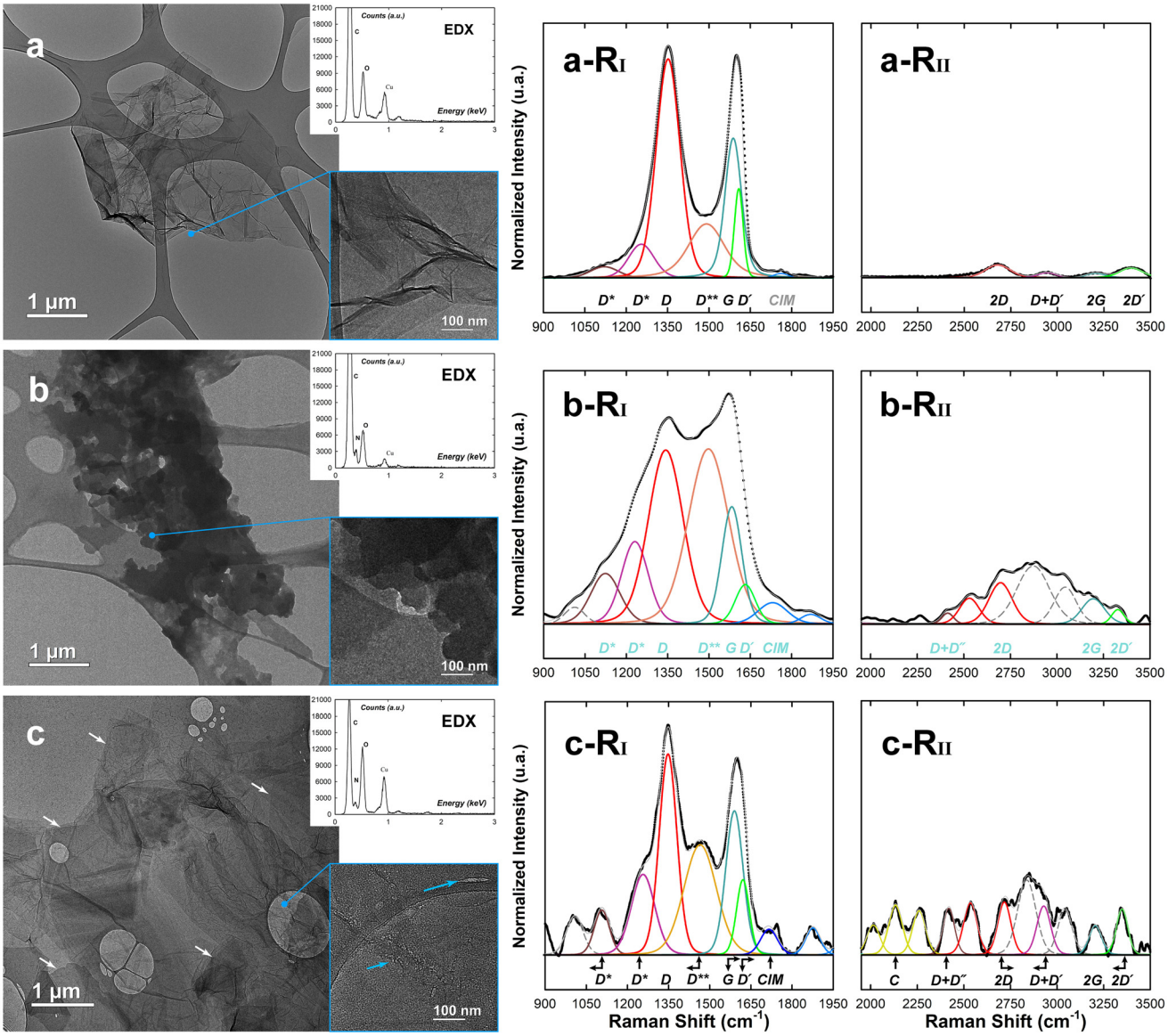

Fig. 1 Morpho-vibrational microscopy results of GO_m, *e*Mel, and GO_m–*e*Mel species. (a–c) BF-TEM low-magnification images of GO_m, *e*Mel, and GO_m–*e*Mel, respectively. Insets: EDX spectra and magnified images of the corresponding compounds. (a–c-R_I) First-order resonance Raman spectra showing the experimental, fitting and deconvolution profiles. (a–c-R_{II}) Second-order resonance Raman spectra showing the experimental, fitting and deconvolution profiles.

of the G and D′ bands were assigned to the peak at about 3205 (2G) and 3395 (2D′) cm^{-1}.

To confirm that the abovementioned signature of phonon modes is related to the presence of localized atomic carbon defects, high-resolution electron imaging of a single micronized GO sheet was carried out, and the results are shown in Fig. 2a. In this regard, the bending, curving, and wrinkling formations in the sheets, which are related to the resonance bands associated with disordered layers, can be directly observed in Fig. 2b. These puckered effects generate reduced structural coherence along the graphene surface due to the random oxide-defect functionalization, which induces a broadening effect in the first-order Raman modes and a weakening of the signal in the overtone modes (Fig. 1a-R_I and -R_{II}). The FFT pattern corresponding to an outer nanoregion of Fig. 2b-I shows the superposition of two hexagonal patterns and other diffraction spots of weaker intensities due to the disorder in the layer stacking. The corresponding inverse FFT shows irregular, wavy, dark lines at the edges separated by 0.39 nm, which is larger than the interlayer spacing in pristine graphite (0.33 nm), suggesting that there are four wavy hexagonal planes. Interestingly, the wavy morphology of the folded sheets affects the resolution of the crystalline lattice fringes between the edge and the stacked layers (red dot line); whereas the inner region clearly shows a crystalline lattice with a Moiré pattern due to the formation of twisting layers. In addition,

farther from the edge, the high intensity of the FFT spots evidences a superimposed 4 layers rotated by 17.3° around the [002] zone axis (inset), and the corresponding IFFT images show a lattice spacing of 0.209 nm, belonging to the (101) reflection plane (Table S2). The direct imaging evidence of bending and twisting in the layers is highly consistent with resonant Raman mechanisms (2D band, Fig. 2a-R_{II}).[32]

Furthermore, the disturbed twisted crystal structures with the presence of island coalescence formation, attributable to strong oxidation interactions (red arrows, IFFT image of Fig. 2b-I), are displayed at high resolution and were analytically measured *via* the vibrational atomic defects (D* and D′ bands, Fig. 2a-R_I). High-resolution imaging of the curving and wrinkling effects is displayed in Fig. 2c. The curved lattice fringes show a spacing of about 0.39 nm, which decreases to reach densely packed sheets of dark intensity (inset, bottom left). This may be attributed to the high amount of hydrogenated sp^3 sites also detected by the resonance D* band. Similarly, the bending, curving, and wrinkling formations of both basal and edge sheets are shown in Fig. 2c-I (green square). The corresponding IFFT image shows an interlayer spacing of 0.41 nm of a possible vertical and expanded sheet edge with dark intensity contrast compared to the surface layers. The presence of vertical edges was also confirmed by the broadening behaviour of the 2D band, which is generated by the polarization direction of the excitation beam, perpendicular to the abundant defect vertical sheets.[18] The opening effects of the micro-sheets due to a possible intercalation of the oxide groups can be related to the measured slight blue-shift of the G_{GOm} band, as previously reported.[33]

Complementary to this, we recorded electron diffraction patterns (EDP) to validate the vibrational data discussed above. Fig. 2d shows the superposition of two EDPs. By measuring the *d*-spacing of the diffraction rings produced by a random orientation of the GO_m layers, the *P*63/*mmc* hexagonal symmetry with preferential crystallographic orientation (101) and higher-order diffraction rings (105 and 201) was identified. The relevant and concomitant absence of (002) planes indicates that GO_m planes perpendicularly intercept the crystallographic *b*-axis (axis parallel to the layers, zone axis [010]), which is an experimental confirmation of the presence of the exposed sharp edge of the vertical GO_m. The second EDP of

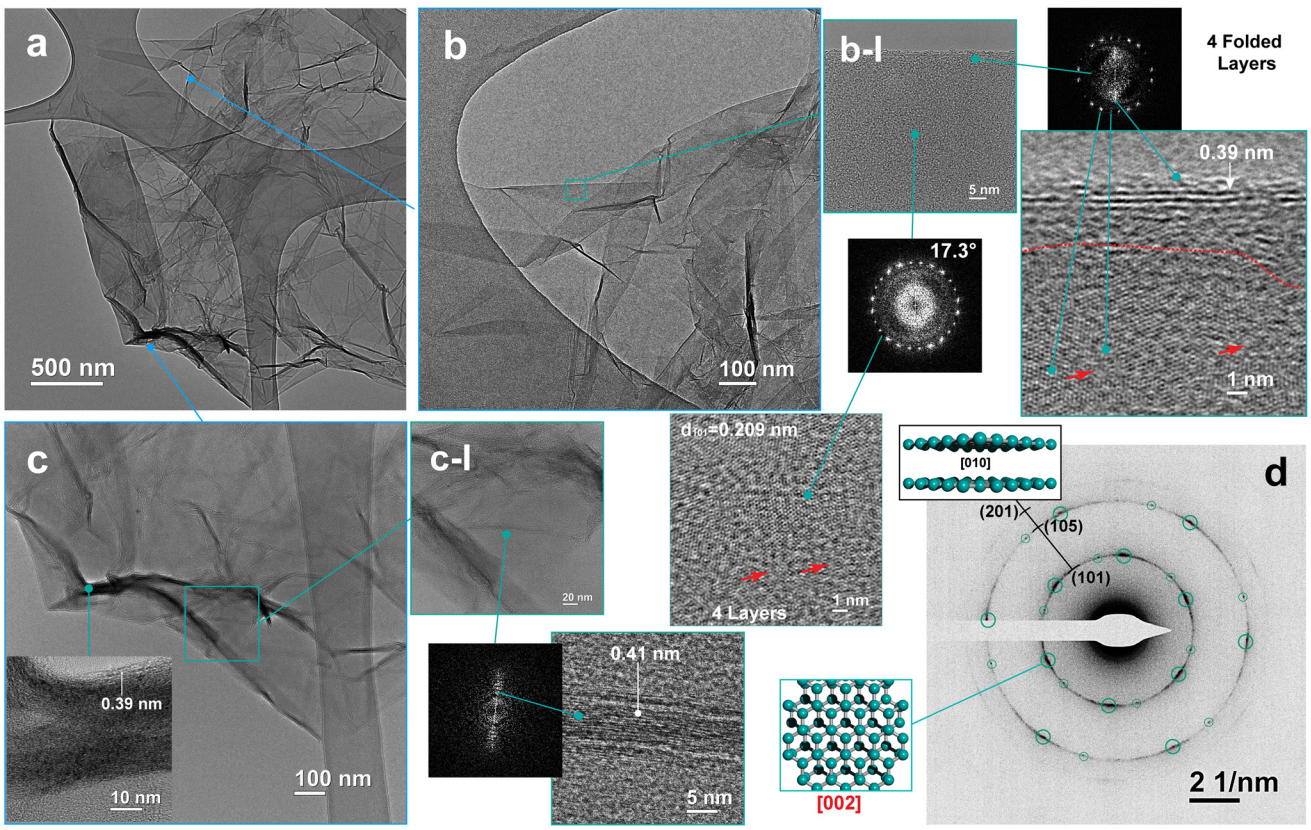

Fig. 2 Morpho-structural observations of GO_m bending, curving and wrinkling formations. (a) BF-TEM image of a graphene oxide sheet. (b) High-magnification TEM image of the GO_m edge (blue square of a). (b-I) High-resolution image of the nano-area of b (green square). Insets: the corresponding FFT patterns of the GO_m hexagonal shape (green dots) over their IFFT images (bottom and right sides). The bottom IFFT image of a nanometric area illustrates the crystalline lattice fringes partially disturbed by oxidation interactions (red arrows). (c) High magnification TEM image of the disordered flakes. (c-I) High-resolution image of the nano-area of c (green square). Insets: vertical multi-layer graphene; high-resolution image of the nano-area of c (green square, left top side); an IFFT image of the nanometric area (green dot) illustrating large crystalline lattice fringes of vertical GO_m. (d) EDP showing distinct rings and diffraction spots belonging to the *P*63/*mmc* hexagonal symmetry of the graphite phase.

ordered diffraction spots with irregular intensity was identified to belong to the six-fold symmetry with a hexagonal structure of AB stacking order (green circles), perpendicularly intercepting the crystallographic *c*-axis (or stacking axis of graphene layers, zone axis [002]), confirming the results in Fig. 2c. These findings confirm that the turbostratic and twisted character of the micronized graphene oxide arises from the presence of highly active defects, which are ideal for a higher catalytic activity.[13]

2.3. Direct evidence of eumelanin nanostructures having a vibrational broad signal

Morphological observations of the *e*Mel biomolecule have shown sheet-like nanostructured microaggregates of irregular shape and size having edges with high roughness (Fig. 1b), and the chemical species present were confirmed by EDX spectroscopy (C, O, and N; inset). The corresponding Raman *e*Mel spectra consisting of broad bandwidths with two main resonant peaks (1343 and 1583 cm^{-1}) suggest a structural disorder of the molecular orientations, having a similar Raman profile to other natural eumelanin (see Fig. 1b-R_I, Table S1).[17] The peak at approximately 1343 cm^{-1} has been assigned mainly to the ν_{as}(C–C) asymmetric stretching modes of the indole-atom rings (less resonance for the ν_{as}(C–N) mode), and to the in-plane δ(O–H) and δ(C–H) with dominant bending.[34] The ensemble of these vibrational modes, aligned in frequency to the D band of the GO_m, can be related to the indole π–π interaction stacking factors of the missing vertical orientation of the *e*Mel units, showing high roughness near the surface sheets (inset of Fig. 1b). The second dominant peak at approximately 1583 cm^{-1}, close to the G_{GOm} band frequency position, has been mainly attributed to the predominant ν_s(C=C) *symmetrical* stretching mode of the phenol ring, similar to the sp^2-hybridization of the carbon oxide system, coupled with the in-plane δ(O–H) mode. The slight red-shift of the G_{eMel} band, compared to the GO_m spectrum, arises from the larger contribution of the vibrational density of states of the isolated sp^2 phenol rings. The in-plane δ(O–H) mode contribution of *e*Mel molecules is greater than that for graphene oxide sites, which have a high surface area to volume ratio. Indeed, the *e*Mel intensity ratio $I_{D/G}$ (0.91) was less than that of GO_m because of a special enhancement factor in graphene oxide on the D_{GOm} mode in the presence of bending and whisker formations, followed by increasing the crystalline planar size *La* of about 21.13 nm for *e*Mel. Similar to the sp^2 hybridization stretching of the GO_m, the middle D** at about 1476 cm^{-1} has been revealed and assigned to the main ν_{ring}(C=C) *asymmetric* stretching mode of the six-atom rings coupled with the in-plane δ(O–H) bending mode.[35] The broader and up-shifted D** band, compared to GO_m, is a peculiar signature of the large vibrational resonance of the carbon and oxygen atomic bonds of the *e*Mel units, having many different orientations with respect to the excitation polarization direction. The vibrational peak at about 1632 cm^{-1} has been assigned to the C–O stretching mode, similar to the GO_m contribution. The vibration of the out of-plane γ(C=C) and γ(O–H) bending modes of the pyrrole structure (~1124 cm^{-1}) can be related to the stretching vibrations of both hydrogenated sp^3 sites, similar to the D^*_{GOm} band. The vibrational peak at about 1231 cm^{-1} has been related to the ν_{rings}(CNC) symmetric stretching modes and in-plane δ(O–H), δ(N–H), and δ(C–H) bending modes.[17] These results indicate that the Raman spectrum originated from the pyrrole and indole rings coupled with the hydroxyl group, generating different bond strengths and vibrational frequencies, all very close to turbostratic graphite oxide flakes.[36] The remaining first-order vibrational peaks at about 1719 and 1869 cm^{-1} are assigned to the ν_{as}(C–N) and ν_s(C=C) stretching modes coupled with the in-plane δ(N–H), δ(C–H), and δ(O–H) bending modes of the indole rings, respectively. Additionally, there are a series of second-order bands, assigned mainly to the C–H stretching mode, which are active near the 2D, 2G, 2D′ bands of the GO_m (2697, 3195, and 3327 cm^{-1}, Fig. 2a-R_{II}). Similarly, the vibrational peaks at about 2419 cm^{-1} can be associated with the D + D″ graphite band, indicating finite-sized crystals (nano-islands).[31] The D + D′ band could not be assigned because of the absence of atomic defects for its activation. Instead, two deconvolution peaks were measured (2873 and 3043 cm^{-1}). To date, significant efforts have been devoted to theoretical research aimed at predicting the structure of eumelanin, comparing its broad Raman bands with well-known organic systems. However, these valuable outcomes lack a crucial connection between the vibrational atomic lengths and the experimental structures under study. Thus, understanding how self-assembling processes generate short-range organized structures is essential for developing strategies to control the physicochemical properties of these biosystems. The use of low-dose high-resolution electron imaging has allowed the detailed analysis of self-assembling eumelanin, as shown in Fig. 3a–c.[19,37]

Bright-field TEM images of *e*Mel reveal irregular micrometric layers with regions of both low and high electron transparency, in contrast to the continuous and transparent micron-sized sheets observed in the defect GOm (Fig. 2a and 3a). This variation in intensity contrast arises from the disordered stacking of self-assembled nanosheets with irregular shapes, shown in Fig. 3a and b (blue arrows). The imaging method used, which is analogous to nanodiffraction, has identified for the first time the different structural behaviours of *e*Mel molecules in two nanoregions of Fig. 3b. The FFT pattern, showing quasi-hexagonal diffraction spots, suggests the presence of ultrathin layers of eumelanin laying on the holey carbon amorphous thin-film support. The FFT pattern has been compared to the electron diffraction simulation from a crystal built considering the space group *P*212121 using the unit-cell parameters calculated by the DFT theoretical model,[38] which is in agreement with the presence of a molecular layer of *e*Mel oriented along the [100] zone axis parallel to the electron beam. Moreover, an extra array of diffraction spots is present in the FFT pattern (inset of FFT, top right side), indicating a missing orientation of the stacked molecular units along the transversal crystalline plane orthogonal to the [100] zone axis. Indeed, the corresponding IFFT image

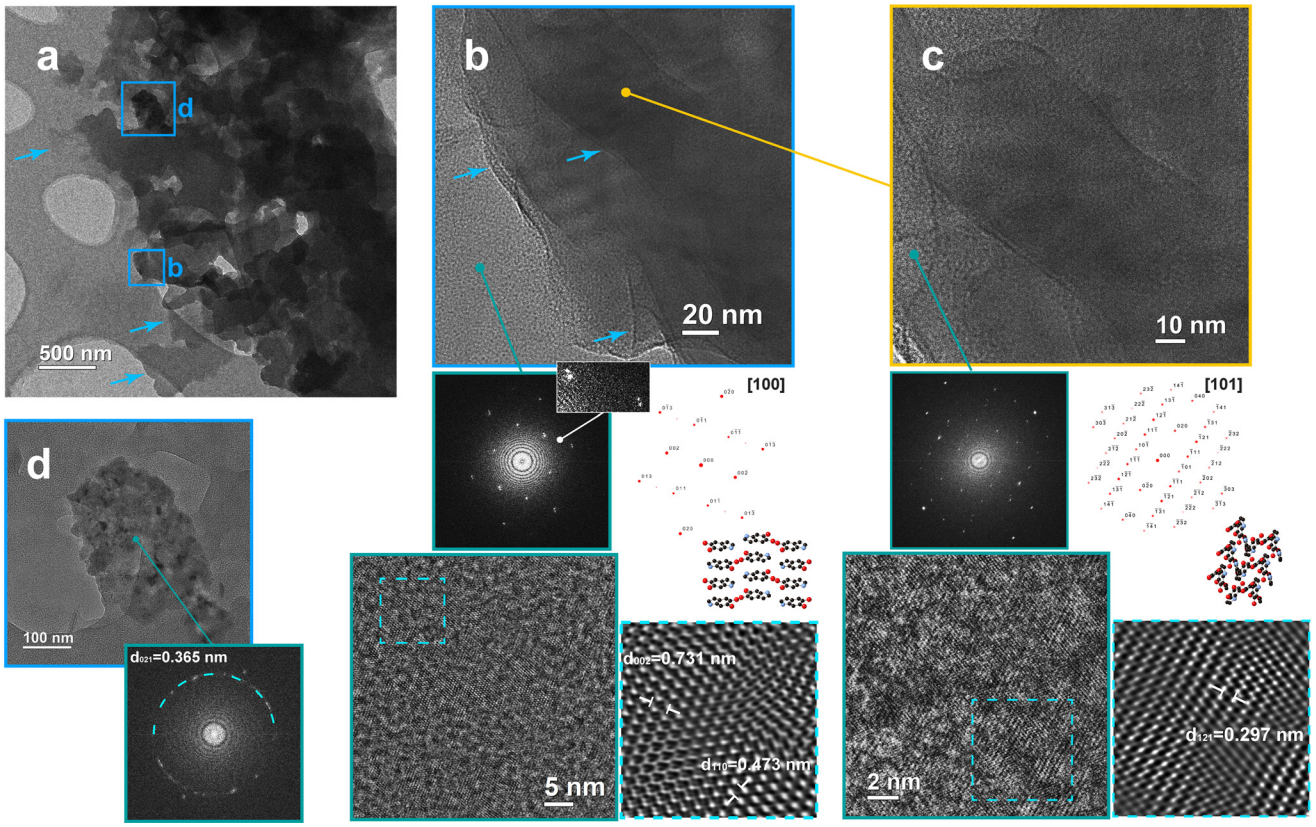

Fig. 3 Morpho-structural observations of the self-aggregation of eumelanin molecules. (a) BF-TEM image of irregular eumelanin nanosheets (blue arrows). (b) High magnification TEM image of the eumelanin layers (blue square in a). Insets: FFT spot pattern of ultrathin eumelanin with quasi-hexagonal shape (green dashed-line); the smallest inset shows an extra array of diffraction spots; identification of FFT diffraction spots by electron diffraction simulation with the [100] zone axis of crystalline eumelanin (below FFT image); high resolution IFFT image of the nanometric area illustrating crystalline lattice fringes (beside the FFT image); amplitude-filtered single frame generated by inverse of the IFFT image and crystalline eumelanin structural model is shown below. (c) High-resolution image of eumelanin in the thin region of b (green spot-line). Insets: FFT spot pattern of c, and its corresponding electron diffraction simulation with the [101] zone axis; high-resolution IFFT image of the nanometric area (green square in c), and its amplitude-filtered single frame illustrating a zig-zag atomic organization confirmed by the structural model below (cyan dot-square). (d) High-magnification imaging of the eumelanin layers (blue square in a) and its corresponding FFT ring pattern of thick eumelanin (cyan dot-arc).

below shows crystalline lattice fringes with different orientations, indicating the short-range order of nanoregions. This finding can be seen more clearly in the amplitude-filtered single frame generated by the inverse of the FFT image (beside) in which lattice fringes have large spacings of 0.731 nm (002) and 0.473 nm (110) compared to the crystalline lattice of GO_m (Table S2). The visible quasi-hexagonal crystalline shapes might be related either to the stacking tilt or disorder of the eumelanin units that validate the measured broad bands at about 1343 cm^{-1}. The hypothesis of the vertical missing orientation of the *e*Mel units attributed to the so-called D_{eMel} band has also been confirmed by analysing another region. On performing FFT scanning, as shown in Fig. 3c, a nanoregion indicates a further pattern of well-organized diffracted spots (green square, and the lower part of Fig. 3c). The electron diffraction simulation identified a different preferential orientation of *e*Mel molecules along the [101] zone axis, wherein the IFFT image shows a zig-zag shape of assembled eumelanin with a crystalline lattice having a spacing of 0.209 nm (blue square of Fig. 3c). This particular shape, not visible in the other near nanoregions, might be related to the edge roughness of *e*Mel nanosheets measured by the disorder-induced D and 2D bands, similar to graphitic materials.[15] It is interesting to note that the change in the crystalline orientations into two different nanoregions (amorphous carbon [100] and eumelanin bulk [100] zone axes) is evidence of the ability of the smallest biomolecule to be structurally modulated by external environmental interactions. This is consistent with the measured broader and up-shifted D** of the *e*Mel nanosheets, confirming the different crystalline orientations under the excitation polarization direction. Indeed, a thick region of eumelanin, showing missing layer formation, indicates the nanocrystalline character of random orientation, confirmed by the derived FFT pattern in Fig. 3d (blue square in Fig. 3a). This confirms the presence of nano-crystalline planes with a high degree of randomly oriented nanostructured complexes of varying units, which might be related to irregular monomer and functional group arrangements of eumelanin. Therefore, the changing dimensions and orientations of the crystalline nanodomains had a strong impact on

the phonon modes; in particular, the series of *e*Mel superstructures had random orientation ([*h*,*k*,0]) and random stacking ([0,0,*l*]) along the crystallographic axes, broadening the Raman spectra (Fig. 2a-R_I and -R_{II}).

2.4. Vibrational and nanoimaging of hybrid biocompatible superstructures

To understand how biomolecular structures may be affected by external nano-environments of an inanimate defect structure, eumelanin molecules were hybridized with the carbon oxide system, shown in Fig. 1c. The micrograph shows the overlapping of micronized multilayers affected by bending, curving, and wrinkling (indicated by white arrows). A magnified nanoregion of the GO_m sheet shows high surface roughness due to the presence of nanostructured objects, which have a slightly brighter contrast, are self-organized in aligned and isolated nanoparticles (marked with blue arrows, inset of Fig. 1c), and are not observed in GO_m (Fig. 1a). The EDX spectra show a more intense oxygen peak, compared to GO_m alone, and a well-defined nitrogen peak related to the observed organic biomolecules (inset of Fig. 1c). This first observation evidences the ability of the smallest *e*Mel to change structurally and morphologically from irregular nano-sheets into nanoparticles, after interacting with disorder-defect micronized GO (Fig. 2).

The corresponding Raman spectra show similar broad bandwidths of the GO_m spectral profile overlapped with peaks of the *e*Mel spectrum, evidencing a limited excess of *e*Mel during the sample fabrication. The first-order peaks of the Raman signals (D*, D, D**, G, D′, and CIM bands) exhibited slight changes in intensity-position-width (Fig. 1c-R_I), while the second-order Raman peak profile evolved with a gradual narrowing of the overtone bands (Fig. 1c-R_{II}). By excluding spurious peaks due to the excitation frequency (532 nm) used, the G band showed a slight downshift towards a higher frequency in GO_m–*e*Mel (1592 *vs.* 1588 cm^{-1}) in spite of the high-intensity, broad G_{eMel} band, followed by narrowing of the D band profile. These resonance scattering behaviours may be attributed to the following competing mechanisms: structural–vibrational reorganization with decreasing doping level compared to defect GO_m; active phonons modes at high frequency due to their confinement of the isolated (C=C) and (O–H) shorter bonds of the smallest biomolecules; atomic reorganization induced in the sp^2 carbon lattice through *e*Mel epoxy and hydroxyl groups, which would mean that a chemical functionalization does indeed occur.[26] However, only a slight decrease in the crystalline planar size *La* of 16.47 nm (*I*(D/G) 1.17) was estimated, indicating a decrease in crystallinity orientations, then a phonon propagation in the GO plane, parallel to the polarization direction of the excitation beam. The crystallinity decrease of this hybrid product might also be correlated to the interactions of *e*Mel units with GO_m, which may reduce the latter's reactive oxygen functionality.[10] In this regard, the red-shifting of the prominent D** band at about 1463 cm^{-1} to that of sp^3 hybridization of the pristine GO_m may be related to the increase in tetrahedral carbon species, generating an augmentation in conformational disorder with the nanometric formation of bio-carbon allotropes. Therefore, the strong interactions of the (O–H) bending mode may be attributed to strong cooperation between *e*Mel and the atomic oxidized defect GO_m, especially on the edge plane (Fig. 4b).

The dominant middle D** band in the GO_m was also assigned to the formation of spherule carbon structures,[39] comparable to our observations of spherule *e*Mel nanoparticles in Fig. 4c and in the inset of Fig. 1c. Indeed, the measured broad and blue-downshifted D′ band (1625 cm^{-1}), previously assigned to the (C–O) vibrational stretching in GO_m, still evidences the presence of biomolecule interactions with vacancy defects on the GO_m surfaces.

The strong interactions between GO_m-*e*Mel are evidenced by an increased intensity of the D* band, with well-separated modes (1107 and 1255 cm^{-1}), which confirms the increased C–C stretching vibrations of both hydrogenated and unhydrogenated sp^3 sites. This hybridization character of covalent interactions between spherical and sheet-like carbon biostructures may be evidenced by the increased intensity modes at about 1719 cm^{-1}, and the peak at 1876 cm^{-1}, which was not measured for GO_m. These Raman peaks, attributed to the Stone–Wales defects,[26] have previously shown similar resonance vibration (1830–1880 cm^{-1}, CIM-band) in a monodimensional carbon system interacting with the surface of different carbon species.[40] High-resolution TEM observations of Fig. 4c (blue arrows) indicate the linear self-aggregation of *e*Mel nanoparticles that interact with the aligned defects along the lattice fringes of wrinkled or puckered GO_m sheets, shown in Fig. 2c-I.

These findings have also been confirmed by comparing the second-order resonance Raman spectra. The GO_m–*e*Mel exhibited well-separated and high-intensity peaks compared to the *e*Mel and GO_m spectra (Fig. 1c-R_{II}). The asymmetric shape of the up-shifted D + D″ band (~2419 cm^{-1}) indicates a change in the electronic structure within the conduction bands for increased *n*-layers of different combinations of phonon wave vectors.[41] This scattering process, slightly measured in the *e*Mel spectra, can be further related to the presence of biomolecule units organized in ultrathin elongated nanosheets of finite-sized crystals (nano-islands),[31] laying on the GO_m surface (inset of Fig. 1c). Interestingly, a double-resonant scattering process exhibited a stronger and narrower 2D band split into two deconvoluted peaks (2535 and 2719 cm^{-1}), one of which was blue-shifted in comparison to that of GO_m (2680 *vs.* 2719 cm^{-1}). These two dominant subcomponents have been assigned in graphene to be related to the increasing number of intercalant layers due to the splitting of electronic bands and phonon branches.[33,42] A further presence of non-aromatic CH groups has been attributed to the spectral region 2800–3000 cm^{-1}, having a strong broad band split into three deconvoluted peaks identified at about 2837, 2928, and 3048 cm^{-1}. The measured D + D′ band, red-shifted with respect to that of GO_m (2944 *vs.* 2928 cm^{-1}), was related to the interesting decrease in reduced atomic defects at the edge of graphene whiskers.[13,18] The appearance of C peaks, composed of three peaks at about 2014, 2156, and 2252 cm^{-1}, not measured in GO_m and in *e*Mel, provides evidence for further

interlayer hybridization, assigned to the stretching modes of sp-hybridized carbon, inducing carbine formation from polymers or hydrocarbons.[43] The high-frequency 2G and 2D′ bands (3205 and 3349 cm^{-1}) were assigned to the stretching vibration of hydroxyl (C–OH) groups.[24]

High resolution imaging clearly shows a dark contrast indicating a few layers of the hybrid GO_m-*e*Mel (Fig. 4a), compared to the highest electron transparency of the pristine GO_m (Fig. 2a). The puckered GO_m–*e*Mel sheets, shown in Fig. 4b (blue arrows), display the irregular and widest lattice fringes of nanostructured eumelanin, linearly distributed along the direction of the curving and exposed edges of the graphene oxide, which were not observed in the pristine GO_m (insets of Fig. 2c). This strong interaction of the GO_m–*e*Mel system may most likely be related to the doping/intercalation with increasing layer numbers and a decrease in the reactive oxygen functionality of GO_m. This has been confirmed by the sensitive Raman spectra through a blue-shift of the G and 2D bands with the narrowing of the $D_{GOm–eMel}$ band (Fig. 1c-R_I and -R_{II}). Yet, from the nanoparticle formation perspective, spherule eumelanin structures appeared with bright intensity contrast compared to the dark GO_m sheets in Fig. 4c, showing bright isolated and aligned nanoparticles of about 3–9 nm in width along the puckered GO_m sheets (blue arrows). This remarkable structural change of the pure eumelanin, extracted from the black soldier fly, previously assembled in irregular nano sheets, and now reassembled in spherical nanoparticles with GO_m, could imply that the molecular units are noncovalently linked without polymeric conformations. The allocated nanoparticle/oxide-layer interactions, similar to the spherule carbon structures, are validated by the prominent, red-shifted D** band. The bright aligned nanoparticles, anchored on the GO_m surface, are validated by the appearance of the second-order C stretching mode (interlayer sp hybridization) and the increased CIM band (1D-carbon surfaces with carbon species). The interesting reduced atomic defects of GO_m due to the interactions with *e*Mel were also confirmed by the slight red-shift of the D + D′ band. These complementary findings suggest that eumelanin molecules are capable of multiple dynamic nano-organizations and mutually interact with the atomic-defect GO_m edge, forming interesting nanoaggregates.

The low-dose experimental electron diffraction results displayed two superimposed diffraction patterns (Fig. 4d). The diffraction spots, belonging to the sixfold symmetry of bilayer

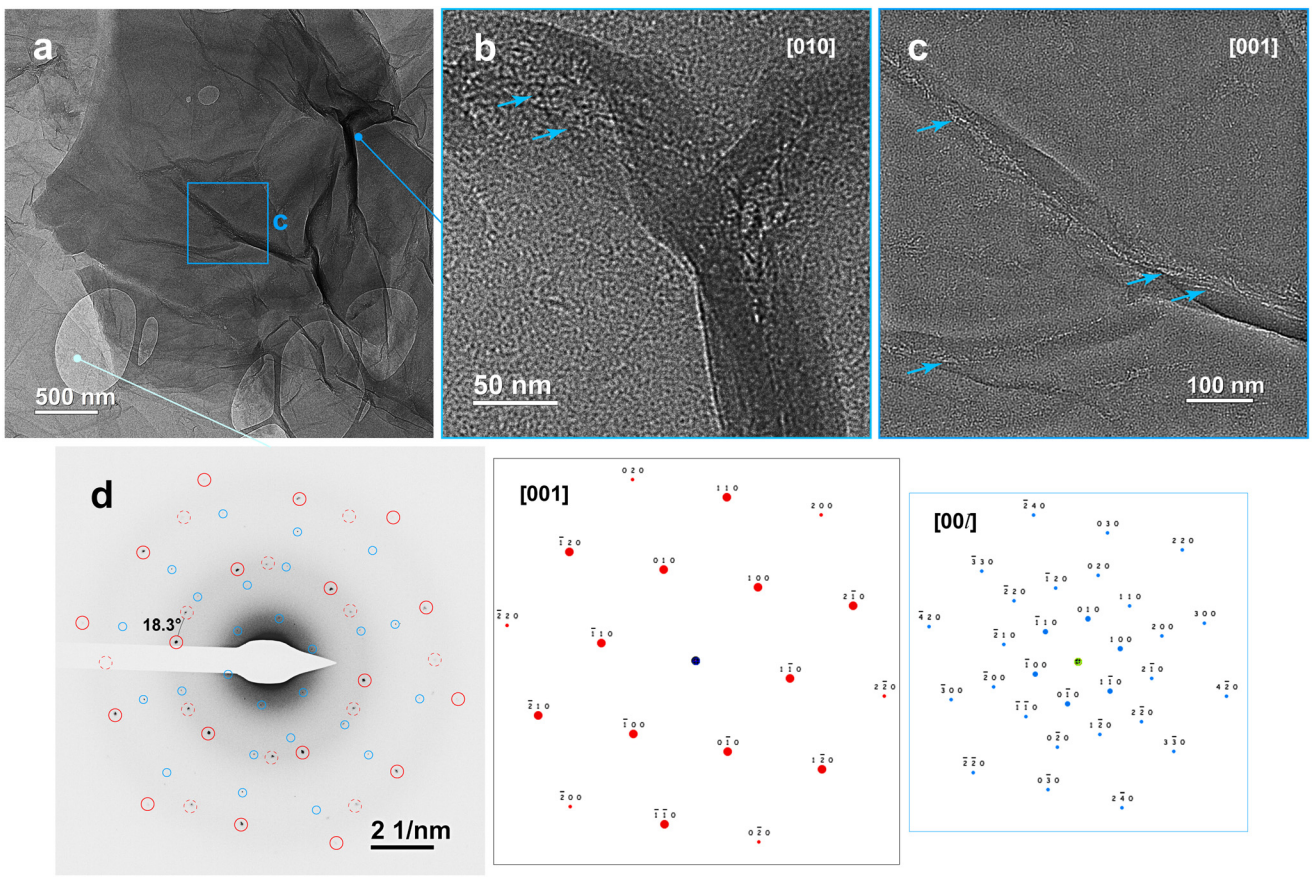

Fig. 4 Morpho-structural observations of eumelanin interacting with graphene oxide sheets. (a) BF-TEM image of graphene oxide sheets. (b) High-resolution image of the bright eumelanin nano-aggregates (blue arrows), interacting on the edge of the vertical graphene oxide. (c) High-magnification image of a nano-area showing bright nano-aggregates of eumelanin aligned along the defect GO_m sheets (blue arrows). (d) EDP taken from a distinct diffraction spot belonging to the *P*63/*mmc* hexagonal symmetry of the graphite phase (black circles) and to the space group $P2_12_12_1$ of crystalline eumelanin (blue circles).

graphene, have been indexed according to the structure of graphite with space *P*63/*mmc* (black arcs, d_{001} = 0.339 nm) and behind the corresponding simulated EDP with zone axis [002], already detected in the EDP of the pristine GO_m (green circles, Fig. 2d). A second stack, still present after *e*Mel interactions, was rotated approximately 18.3 degrees around the [002] zone axis (black dot circle), in agreement with the corresponding intense 2D Raman band. Interestingly, some additional spots, closer to the central spot, exhibited a further six-fold symmetry with first-order hexagonal spots more intense than the higher orders, confirming the presence of a further layer in the stacking configuration.[44] The measured *d*-spacing of 0.776 nm is slightly higher than the (001) crystallographic plane of crystalline eumelanin with the space group *P*212121. Therefore, the increased interlayer spacing between GO_m sheets along the crystallographic stacking *c*-axis may be attributed to an organophilization of the eumelanin molecules through the reduction of oxidized carbon functional groups on the basal planes and edges of GO_m.[45] Yet, from complementary perspectives, this is in agreement with hybrid intercalated layer formations inducing random stacking ([0,0,*l*]) along the crystallographic *c*-axis, such that the narrowing 2D increment and D modes do indeed occur (Fig. 1c-R_I and -R_{II}).[42,46] Moreover, the re-organization of the vacancy defects due to the doping/intercalation variation is in agreement with the shifts in the G and D′ bands to high frequencies.[33] This strong covalent interaction between spherical/sheet carbon biostructures has also worked like a functionalization/reduction of the oxidation product coverage at the atomic defects of GO_m, which might cause an increase in conductivity.[9]

3. Conclusions

Our work presents experimental imaging/analytical evidence that challenges the traditional understanding of the self-assembling behaviour of eumelanin superstructures, depending not only on the contact area but also on the shape of domain engagements. We have demonstrated that the interfacial contacts of the micronized graphene oxide sheets cause effective morpho-structural changes in eumelanin, from their naturally occurring irregular short-range order domains to form diverse superstructures with the biocompatible carbon oxide substrate. The experimental approach demonstrates the efficacy of using conventional vibrational resonance micro-Raman and high-resolution electron microscopies, which complement each other in determining the morphologies of these complex structures (Fig. 1). The integration of conventional Raman spectroscopy with HRTEM for complementary vibrational-structure analysis has confirmed the presence of different structural organizations of GO_m sheet deformations modulated by carbon/oxygen atomic defect sites on both the surface and the expanded edges of vertical sheets (Fig. 2). The direct electron imaging of the atomic defects on the irregular surface (D′ and 2D bands), and the abundant defects at the edges of vertical sheets (broad D* band), provides more information when complemented with the sensitive Raman spectra. The assembly formations, involving twisting (2D band), wrinkling (D + D′ band), folding (D band), and intercalation (blue-shifted G band) of the irregular GO_m sheets, have been validated by high-resolution imaging. In this regard, the sensitive vibrational mode analysis validates the chemical actions of both sp^2-hybridization involving the bending of hydrogenated-oxide functional groups (G and D* bands), and sp^3 sites localized at the observed expanded edges (D** band).

The relevance of vibrational-structure characterization is also evident in the investigation of eumelanin superstructures, which showed the behaviour of the Raman spectra related to carbon, oxygen, hydrogen (and nitrogen) vibrational bonds. The corresponding broadening of the D band (associated with an intrinsic high disorder of the system) and G band (an indicator of an irregular stacking structure), which were similar in frequency to the GO_m Raman bands, represent the dominant vibrational modes. These analytical results have been quantitatively validated for the first time through high-resolution nano-diffraction/imaging, confirming the poor structural character of the eumelanin units as predicted by Raman band analysis. The assembled superstructures have shown irregularly stacked nanosheets composed of very small nanocrystalline domains exhibiting distinct orientations in response to the order/disorder of the surrounding interactions (zig-zag and quasi-hexagonal lattice fringe shapes, Fig. 3). This finding strongly impacts the phonon modes, which are strictly dependent on the dimensions and the random orientation ([*h*,*k*,0]) and random stacking ([0,0,*l*]) along the crystallographic axes, resulting in multi-resonance broadening of the Raman spectral bands.

In our efforts to create manipulated routes of the eumelanin units, we have shown that the micronized GO sheets exhibit notable control over the eumelanin units in aqueous solution at room temperature. For the first time, the *e*Mel superstructures have demonstrated the ability to disassemble irregular nanosheets and reassemble into nanoscopic spherule particles, which also evolved into an elongated shape, confined on the defective functional surface of the GO_m substrate (Fig. 4). To overcome the limitations of HRTEM in imaging the crystalline lattices of soft *e*Mel, the sensitive Raman spectra were employed, which clearly revealed changes in the $G_{GOm-eMel}$ and $D_{GOm-eMel}$ bands. This structural–vibrational change confirmed an increase in resonant shorter bonds (C=C and O–H) within *e*Mel, followed by a decrease in the reactive functionality of the GO_m substrate (Fig. 1c-R_I). Furthermore, the red-shifted D** band supports the strong cooperation between *e*Mel and GO_m, with the formation of spherule and elongated graphitic structures. In this regard, the possible doping/intercalation of *e*Mel between GO_m sheets influenced the G and 2D bands, as confirmed by the increased interlayer spacing observed through electron diffraction analysis (Fig. 4d). With regard to manipulating small biomaterials, the use of Raman-HRTEM complements existing strategies for revealing the strong affinity of self-assembly between carbon oxide layers and biological matter that does not require

manual operations. This biocompatibility affinity suggests potential strategies for preserving the native state of small biomolecules upon adsorption onto appropriately engineered 2D materials in aqueous dispersion. The confirmed disassembly of nanostructured *e*Mel with decreasing the dimensions to nanometric units leads to a size-dependent transition from continuous to discrete energy levels, thereby enhancing quantum yield. Regarding the hybrid integration, the electronic structures of the GO_m might be altered by inducing *biomolecule defects*, thus creating a new bandgap-tunable opening. Such variations in energy levels may reduce the effective bandgap of the bulk GO_m–*e*Mel hybrid material, significantly influencing their cross-correlated photophysical and photochemical properties. These effects will be highly relevant for practical applications in surface coatings, biosensing, and radiation protection.[47] Therefore, these results provide concrete information on key scientific aspects in helping sustainable research towards the eventual control of small biomolecules, which may have practical implications for graphene-based nanofabrication technologies with applications in environmental science and biomedicine.

4. Experimental procedures

4.1. Sample fabrication

Graphene oxide (GO) was synthesized using micronized natural graphite with 99.5% purity and a d_{50} of approximately 10 μm, following a modified Hummers' method. The reagents used included sulfuric acid (H_2SO_4, 99%), potassium permanganate ($KMnO_4$, 99%), hydrogen peroxide (H_2O_2, 30%, Fmaia), and hydrochloric acid (HCl, Synth). The synthesis was primarily based on Hummers' method, ensuring that the temperature did not exceed 20 °C during the addition of H_2SO_4 and $KMnO_4$. In a beaker placed in an ice bath, 25 mL of concentrated H_2SO_4 and 1.0 g of graphite were first mixed under constant magnetic stirring. Afterwards, 3 g of $KMnO_4$ was slowly added to the mixture. After 3 hours of stirring, 50 mL of distilled water was added dropwise while maintaining the temperature below 50 °C, keeping the beaker in the ice bath. During this step, the dispersion color changed from black to dark brown. Next, 100 mL of distilled water was added, followed by the addition of 5 mL of H_2O_2 at room temperature to remove any excess $KMnO_4$ and stop the oxidation process. This change in the dispersion color from dark brown to greyish-green indicated the termination of the reaction. To purify the solution, 250 mL of a 30% v/v HCl solution was added, followed by centrifugation at 6000 rpm for 15 minutes. The samples were washed with distilled water and centrifuged multiple times until the pH of the dispersion reached approximately 6 (four washes). Chemical functionalization and doping of micronized GO were determined and characterized using transmission FTIR and XPS spectra (see the SI).

BSF eumelanin powder was provided by Insectta Pte. Ltd for research purposes. The material is produced *via* a patented extraction process from the black soldier fly (*Hermetia illucens*).[48] The BSF eumelanin and GO_m suspensions were prepared separately by dissolving the powder in distilled water with a concentration of 10 mg mL^{-1}. The GO_m–*e*Mel suspensions were mixed all at once, starting from the previous solutions, by mixing 1 mL of BSF eumelanin with 1 mL of GO_m at room temperature.[49]

4.2. Raman scattering experiments

The samples were deposited on FTO glass substrates by drop casting, and Raman spectra of all samples were collected at room temperature in the range 100–3500 cm^{-1} using a probing light source with a 532 nm green laser, a diffraction grating of 600 lines per mm, and a 100× objective. The laser power was 10 mW or less to minimise damage to the samples. The HORIBA IHR320 micro-Raman Scattering system (Horiba, Palaiseau, France) was used, which was equipped with an Olympus BXF41 optical microscope model with 5×, 20×, 50×, and 100× objectives (Olympus, Münster, Germany). After baseline correction and normalization, the contribution of the possible Raman scattering band was determined by curve deconvolution and peak fitting, using the Voigt deconvolution method on the entire Raman profile.[50] The deconvoluted peaks at 560 and 1098 cm^{-1} were excluded in the scattering analysis due to their FTO substrate contributions.

4.3. High-resolution transmission electron microscopy

HR-TEM images were acquired using an FEI Talos F200S Field Emission Gun (FEG) microscope operating @ 200 keV, for samples deposited on a Cu-support grid coated with a holey carbon amorphous film. Energy dispersive X-ray spectroscopy (EDX) compositional analysis maps were collected using a Super-X energy dispersive X-ray spectrometry system, which includes two silicon drift detectors, coupled to the microscope in the Scanning Transmission Electron Microscopy (STEM) mode, using spatial drift correction and a dwell time of 0.2 s. To avoid the occurrence of any fake structural information, we were forced to perform fast image acquisition using minimum dose techniques to prevent electron beam-induced damage to the organic species.[51] To determine the real possibility of strong molecular interactions of the hybrid system, the GO_m–*e*Mel biomaterial was further diluted with distilled water and subjected to soft sonication to remove the excess biomolecules before negative-staining HRTEM observations.[46]

Author contributions

Roberto Matassa: conceptualization, formal analysis, funding acquisition, investigation, methodology, resource, supervision, validation, visualization, writing – original draft, writing – review & editing. Sara Mattiello: conceptualization, formal analysis, investigation, writing – review & editing. Gustavo Guerriero Candido Soares: investigation, writing – review & editing. Juan G. Lozano: funding acquisition, investigation, resource, validation, visualization, writing – review & editing. Ana M. Beltran: funding acquisition, validation, investigation,

resource, writing – review & editing. Costantino Zazza and Nico Sanna: writing – review & editing. Jun Wei Phua: resource, writing – review & editing. Jose Mauricio Rosolen: funding acquisition, investigation, validation, visualization, resource, writing – review & editing. Andrea Di Cicco: funding acquisition, resource, writing – review & editing. Javad Rezvani: writing – review & editing. Roberto Gunnella: conceptualization, funding acquisition, investigation, methodology, resource, supervision, validation, writing – review & editing.

Data availability

All data generated or analyzed during this study are included in the published article and its supplementary information (SI). Supplementary information is available. See DOI: **https://doi.org/10.1039/d5nr02546j**.

Conflicts of interest

Jun Wei Phua holds shares in Insectta Pte. Ltd, which owns patents related to the extraction of eumelanin from black soldier flies.

Acknowledgements

The authors acknowledge the financial support from the National Quantum Science Technology Institute within PNRR MUR project PE0000023-*NQSTI*. Author Roberto Gunella has been funded by the European Union-NextGenerationEU, Mission 4, Component 2, under the Italian Ministry of University and Research (MUR) National Innovation Ecosystem grant ECS00000041 - VITALITY - CUP J13C22000430001. The authors are grateful to the Centro de Investigación, Tecnología e Innovación de la Universidad de Sevilla (*CITIUS*) for the provision of their facilities and expertise. Jose Mauricio Rosolen acknowledges the financial support from FAPESP-Fundação de Amparo a Pesquisa do Estado de São Paulo grant 20/12204-3 and Conselho Nacional de Pesquisa-CNPq: 311647/2021-9. Costantino Zazza and Nico Sanna are supported by the Rome Technopole foundation within the PNRR action in the field of the NextGenerationEU – Section 4. "Digital, Industry and Aerospace" and Flagship Project 5 (FP5) – THz vibrations in Transparent Conducting Oxides project – action.

References

1 V. Karthick, L. Kumar, L. K. Shrestha, V. G. Kumar, P. Pranjali, D. Kumar, A. Pal and K. Ariga, Nanoarchitectonics horizons: materials for life sciences, *Nanoscale*, 2022, **14**, 10630–10647, DOI: **10.1039/D2NR02293A**.

2 M. T. Campos, L. S. Pires, F. D. Magalhães, M. J. Oliveira and A. M. Pinto, Self-assembled inorganic nanomaterials for biomedical applications, *Nanoscale*, 2025, **17**, 5526–5570, DOI: **10.1039/D4NR04537H**.

3 P. Meredith, B. J. Powell, J. Riesz, S. P. Nighswander-Rempel, M. R. Pederson and E. G. Moore, Towards structure-property-function relationships for eumelanin, *Soft Matter*, 2006, **2**(1), 37–44, DOI: **10.1039/b511922g**.

4 J. Cheng, S. C. Moss and M. Eisner, X-ray characterization of melanins-II, *Pigm. Cell Res.*, 1994, **7**(4), 263–273, DOI: **10.1111/j.1600-0749.1994.tb00061.x**.

5 K. C. Littrell, J. M. Gallas, G. W. Zajac and P. Thiyagarajan, Structural studies of bleached melanin by synchrotron small-angle X-ray scattering, *Photochem. Photobiol.*, 2003, **77**(2), 115–120, DOI: **10.1562/0031-8655(2003)077<0115:ssobmb>2.0.co;2**.

6 B. J. Powell, T. Baruah, N. Bernstein, K. Brake, R. H. McKenzie, P. Meredith and M. R. Pederson, A first-principles density-functional calculation of the electronic and vibrational structure of the key melanin monomers, *J. Chem. Phys.*, 2004, **120**, 8608–8615, DOI: **10.1063/1.1690758**, PMID: 15267788.

7 J. I. Paredes and S. Villar-Rodil, Biomolecule-assisted exfoliation and dispersion of graphene and other two-dimensional materials: a review of recent progress and applications, *Nanoscale*, 2016, **8**, 15389–15413, DOI: **10.1039/C6NR02039A**.

8 A. C. Ferrari, F. Bonaccorso, V. Fal'ko, K. S. Novoselov, S. Roche, *et al.*, Science and technology roadmap for graphene, related two-dimensional crystals, and hybrid systems, *Nanoscale*, 2015, **7**, 4598–4810, DOI: **10.1039/C4NR01600A**.

9 N. Al-Shamery, X. Gong, C. Dosche, A. Gupta, M. W. Ming Tan, J. W. Phua and P. S. Lee, Sustainable organic electrodes using black soldier fly-derived melanin for zinc-ion hybrid capacitors, *Commun. Mater.*, 2024, **5**, 156, DOI: **10.1038/s43246-024-00602-4**.

10 D. R. Dreyer, S. Park, C. W. Bielawski and R. S. Ruoff, The chemistry of graphene oxide, *Chem. Soc. Rev.*, 2010, **39**, 228–240, DOI: **10.1039/b917103g**.

11 L. G. Cançado, M. A. Pimenta, B. R. Neves, M. S. Dantas and A. Jorio, Influence of the atomic structure on the Raman spectra of graphite edges, *Phys. Rev. Lett.*, 2004, **93**, 247401, DOI: **10.1103/PhysRevLett.93.247401**.

12 J. C. Meyer, C. O. Girit, M. F. Crommie and A. Zettl, Imaging and dynamics of light atoms and molecules on graphene, *Nature*, 2008, **454**, 319–322, DOI: **10.1038/nature07094**.

13 S. Politi, R. Carcione, E. Tamburri, R. Matassa, T. Lavecchia, M. Angjellari and M. L. Terranova, Graphene platelets from shungite rock modulate electropolymerization and charge storage mechanisms of soft-template synthetized polypyrrole-based nanocomposites, *Sci. Rep.*, 2018, **8**(1), 17045, DOI: **10.1038/s41598-018-35415-2**.

14 L. G. Cançado, A. Jorio, E. H. Ferreira, F. Stavale, C. A. Achete, R. B. Capaz, M. V. Moutinho, A. Lombardo, T. S. Kulmala and A. C. Ferrari, Quantifying defects in graphene via Raman spectroscopy at different excitation ener-

gies, *Nano Lett.*, 2011, **11**, 3190–3196, DOI: 10.1021/nl201432g.

15 M. A. Pimenta, G. Dresselhaus, M. S. Dresselhaus, L. G. Cançado, A. Jorio and R. Saito, Studying disorder in graphite-based systems by Raman spectroscopy, *Phys. Chem. Chem. Phys.*, 2007, **9**, 1276–1291, DOI: 10.1039/b613962k.

16 A. B. Mostert, S. Mattiello, S. Li, G. Perna, M. Lasalvia, P. F. Ambrico, J. V. Paulin, J. V. M. Lima, C. F. O. Graeff, J. W. Phua, M. Matta, A. J. Surman, R. Gunnella and M. Ambrico, Exploring the chemistry and composition of black soldier fly eumelanin, a material for a circular economy, *Mater. Adv.*, 2024, **5**, 8986–8999, DOI: 10.1039/d4ma00825a.

17 G. Perna, M. Lasalvia and V. Capozzi, Vibrational spectroscopy of synthetic and natural eumelanin, *Polym. Int.*, 2016, **65**, 1323–1330, DOI: 10.1002/pi.5182.

18 P. Tan, C. Hu, J. Dong, W. Shen and B. Zhang, Polarization properties, high-order Raman spectra, and frequency asymmetry between Stokes and anti-Stokes scattering of Raman modes in a graphite whisker, *Phys. Rev. B: Condens. Matter Mater. Phys.*, 2001, **64**, 214301–214313.

19 S. Cerra, T. A. Salamone, F. Sciubba, M. Marsotto, C. Battocchio, S. Nappini, F. A. Scaramuzzo, R. Li Voti, C. Sibilia, R. Matassa, A. M. Beltrán, G. Familiari and I. Fratoddi, Study of the interaction mechanism between hydrophilic thiol capped gold nanoparticles and melamine in aqueous medium, *Colloids Surf., B*, 2021, **203**, 111727, DOI: 10.1016/j.colsurfb.2021.111727.

20 R. Matassa, G. Familiari, E. Battaglione, C. Sibilia, G. Leahu, A. Belardini, I. Venditti, L. Fontana and I. Fratoddi, Electron microscopy reveals a soluble hybrid network of individual nanocrystals self-anchored by bifunctional thiol fluorescent bridges, *Nanoscale*, 2016, **8**(42), 18161–18169, DOI: 10.1039/c6nr06260a.

21 R. Li Voti, G. Leahu, C. Sibilia, R. Matassa, G. Familiari, S. Cerra, T. A. Salamone and I. Fratoddi, Photoacoustics for Listening to Metal Nanoparticle Super-Aggregates, *Nanoscale Adv.*, 2021, **3**, 4692–4701, DOI: 10.1039/D1NA00333J.

22 G. Reina, E. Tamburri, S. Orlanducci, S. Gay, R. Matassa, V. Guglielmotti, T. Lavecchia and M. L. Terranova, Nanocarbon surfaces for biomedicine, *Biomatter*, 2014, **4**, e28537, DOI: 10.4161/biom.28537.

23 R. Matassa, S. Orlanducci, G. Reina, M. C. Cassani, D. Passeri and M. L. Terranova, Structural and morphological peculiarities of hybrid Au/nanodiamond engineered nanostructures, *Sci. Rep.*, 2016, **12**(6), 31163, DOI: 10.1038/srep31163.

24 A. Y. Lee, K. Yang, N. D. Anh, C. Park, S. M. Lee, T. G. Lee and M. S. Jeong, Raman Study of D* Band in Graphene Oxide and Its Correlation with Reduction, *Appl. Surf. Sci.*, 2021, **536**, 147990, DOI: 10.1016/j.apsusc.2020.147990.

25 M. Nakamizo and K. Tamai, Raman spectra of the oxidized and polished surfaces of carbon, *Carbon*, 1984, **22**(2), 197–198.

26 K. N. Kudin, B. Ozbas, H. C. Schniepp, R. K. Prud'homme, I. A. Aksay and R. Car, Raman spectra of graphite oxide and functionalized graphene sheets, *Nano Lett.*, 2008, **8**, 36–41, DOI: 10.1021/nl071822y.

27 A. C. Ferrari and J. Robertson, Interpretation of Raman spectra of disordered and amorphous carbon, *Phys. Rev. B: Condens. Matter Mater. Phys.*, 2000, **61**, 14095, DOI: 10.1103/PhysRevB.61.14095.

28 J. Robertson, Amorphous carbon, *Curr. Opin. Solid State Mater. Sci.*, 1996, **1**, 557–561, DOI: 10.1016/S1359-0286(96)80072-6.

29 G. Adamopoulos, K. W. R. Gilkes, J. Robertson, N. M. J. Conway, B. Y. Kleinsorge, A. Buckley and D. N. Batchelder, Ultraviolet Raman characterisation of diamond-like carbon films, *Diamond Relat. Mater.*, 1999, **8**, 541–544.

30 Y. Kawashima and G. Katagiri, Fundamentals, overtones, and combinations in the Raman spectrum of graphite, *Phys. Rev. B: Condens. Matter Mater. Phys.*, 1995, **52**(14), 10053, DOI: 10.1103/PhysRevB.52.10053.

31 A. C. Ferrari and D. M. Basko, Raman Spectroscopy as a Versatile Tool for Studying the Properties of Graphene, *Nat. Nanotechnol.*, 2014, **8**, 235–246.

32 K. Kim, S. Coh, L. Z. Tan, W. Regan, J. M. Yuk, E. Chatterjee, M. F. Crommie, M. L. Cohen, S. G. Louie and A. Zettl, Raman spectroscopy study of rotated double-layer graphene: misorientation-angle dependence of electronic structure, *Phys. Rev. Lett.*, 2012, **108**, 246103, DOI: 10.1103/PhysRevLett.108.246103.

33 W. Zhao, P. H. Tan, J. Liu and A. C. Ferrari, Intercalation of few-layer graphite flakes with $FeCl_3$: Raman determination of Fermi level, layer by layer decoupling, and stability, *J. Am. Chem. Soc.*, 2011, **133**, 5941–5946, DOI: 10.1021/ja110939a.

34 V. Capozzi, G. Perna, A. Gallone, P. F. Biagi, P. Carmone, A. Fratello, G. Guida, P. Zanna and R. J. Cicero, Raman and optical spectroscopy of eumelanin films, *J. Mol. Struct.*, 2005, **744**, 717–721, DOI: 10.1016/j.molstruc.2004.11.074.

35 M. L. Roldán, S. A. Centeno and A. Rizzo, An improved methodology for the characterization and identification of sepia in works of art by normal Raman and SERS, complemented by FTIR, Py-GC/MS, and XRF, *J. Raman Spectrosc.*, 2014, **45**, 1160–1171, DOI: 10.1002/jrs.4620.

36 A. Kaniyoor and S. Ramaprabhu, A Raman spectroscopic investigation of graphite oxide derived graphene, *AIP Adv.*, 2012, **2**, 032183, DOI: 10.1063/1.4756995.

37 S. Cerra, R. Matassa, A. M. Beltrán, G. Familiari, C. Battocchio, I. Pis, F. Sciubba, F. A. Scaramuzzo, A. Del Giudice and I. Fratoddi, Insights about the interaction of methotrexate loaded hydrophilic gold nanoparticles: Spectroscopic, morphological and structural characterizations, *Mater. Sci. Eng., C*, 2020, **117**, 111337, DOI: 10.1016/j.msec.2020.111337.

38 D. Sasikumar, K. Vinod, J. Sunny and M. Hariharan, Exciton interactions in helical crystals of a hydrogen-

bonded eumelanin monomer, *Chem. Sci.*, 2022, **13**(8), 2331–2338, DOI: **10.1039/d1sc06755a**.

39 Z. Q. Yang, J. Verbeeck, D. Schryvers, N. Tarcea, J. Popp and W. Rösler, TEM and Raman characterisation of diamond micro- and nanostructures in carbon spherules from upper soils, *Diamond Relat. Mater.*, 2008, **17**, 937–943.

40 M. Endo, Y. A. Kim, T. Hayashi, H. Muramatsu, M. Terrones, R. Saito, F. Villalpando-Paez, S. G. Chou and M. S. Dresselhaus, Nanotube coalescence-inducing mode: a novel vibrational mode in carbon systems, *Small*, 2006, **2**(8–9), 1031–1036, DOI: **10.1002/smll.200600087**.

41 P. May, M. Lazzeri, P. Venezuela, F. Herziger, G. Callsen, J. S. Reparaz, A. Hoffmann, F. Mauri and J. Maultzsch, Signature of the two-dimensional phonon dispersion in graphene probed by double-resonant Raman scattering, *Phys. Rev. B: Condens. Matter Mater. Phys.*, 2013, **87**, 075402, DOI: **10.1103/PhysRevB.87.075402**.

42 D. Graf, F. Molitor, K. Ensslin, C. Stampfer, A. Jungen, C. Hierold and L. Wirtz, Spatially resolved Raman spectroscopy of single- and few-layer graphene, *Nano Lett.*, 2007, **7**(2), 238–242, DOI: **10.1021/nl061702a**.

43 L. Ravagnan, F. Siviero, C. Lenardi, P. Piseri, E. Barborini, P. Milani, C. S. Casari, A. Li Bassi and C. E. Bottani, Cluster-beam deposition and in situ characterization of carbyne-rich carbon films, *Phys. Rev. Lett.*, **89**, 285506, DOI: **10.1103/PhysRevLett.89.285506**.

44 Y. Hernandez, V. Nicolosi, M. Lotya, F. M. Blighe, Z. Sun, S. De, I. T. McGovern, B. Holland, M. Byrne, Y. K. Gun'Ko, J. J. Boland, P. Niraj, G. Duesberg, S. Krishnamurthy, R. Goodhue, J. Hutchison, V. Scardaci, A. C. Ferrari and J. N. Coleman, High-yield production of graphene by liquid-phase exfoliation of graphite, *Nat. Nanotechnol.*, 2008, **9**, 563–568, DOI: **10.1038/nnano.2008.215**.

45 J. Lee, C. Kim, J. Y. Cheong and I. D. Kim, An angstrom-level *d*-spacing control of graphite oxide using organofillers for high-rate lithium storage, *Chem*, 2022, **8**, 2393–2409, DOI: **10.1016/j.chempr.2022.05.002**.

46 I. O. Maciel, N. Anderson, M. A. Pimenta, A. Hartschuh, H. Qian, M. Terrones, H. Terrones, J. Campos-Delgado, A. M. Rao, L. Novotny and A. Jorio, Electron and phonon renormalization near charged defects in carbon nanotubes, *Nat. Mater.*, 2008, **7**(11), 878–883, DOI: **10.1038/nmat2296**.

47 D. Li, W. Zhang, X. Yu, Z. Wang, Z. Su and G. Wei, When biomolecules meet graphene: from molecular level interactions to material design and applications, *Nanoscale*, 2016, **8**, 19491–19509, DOI: **10.1039/c6nr07249f**.

48 J. W. Phua and C. Ottenheim, *US Patent* US20230127563A1, 2023.

49 M. Ambrico, A. B. Mostert, P. F. Ambrico, J. W. Phua, S. Mattiello and R. Gunnella, Exploring ion mobility mechanisms in poly indolequinone polymers: a case study on black soldier fly melanin, *J. Phys. D: Appl. Phys.*, 2024, **57**, 265303, DOI: **10.1088/1361-6463/ad3765**.

50 K. S. Lee, Z. Landry, F. C. Pereira, M. Wagner, D. Berry, W. E. Huang, G. T. Taylor, J. Kneipp, J. Popp, M. Zhang, J. X. Cheng and R. Stocker, Raman microspectroscopy for microbiology, *Nat. Rev. Methods Primers*, 2021, **1**, 79.

51 R. Matassa, M. Gatti, M. Crociati, R. Brunelli, E. Battaglione, M. Papi, M. De Spirito, S. A. Nottola and G. Familiari, Self-assembly of glycoprotein nanostructured filaments for modulating extracellular networks at long range, *Nanoscale*, 2023, **15**, 17972–17986, DOI: **10.1039/d3nr02644b**.